

Full paper

Triboelectrification-enabled touch sensing for self-powered position mapping and dynamic tracking by a flexible and area-scalable sensor array



Xiao Xiao Zhu^{a,b,c}, Xian Song Meng^{a,b,c}, Shuang Yang Kuang^{a,b,c}, Xian Di Wang^{a,b},
Cao Feng Pan^{a,b}, Guang Zhu^{a,b,*}, Zhong Lin Wang^{a,b,d,*}

^a Beijing Institute of Nanoenergy and Nanosystems, Chinese Academy of Sciences, Beijing 100083, China

^b CAS Center for Excellence in Nanoscience, National Center for Nanoscience and Technology (NCNST), Beijing 100190, China

^c University of Chinese Academy of Sciences, Beijing 100049, China

^d School of Materials Science and Engineering, Georgia Institute of Technology, Atlanta, GA 30332, USA

ARTICLE INFO

Keywords:

Touch sensor
Triboelectrification
Energy conversion
Sensor array
Image mapping

ABSTRACT

A touch sensor is essentially a transducer that transforms physical touches into measurable electric signals. Here, we report a fabric-based self-powered triboelectric sensor array. Individual sensing units are constituted by intersections between row electrode lines and column electrode lines that have complementary patterns. When a sensing unit is touched, surface triboelectrification coupled with electrostatic induction generates an output voltage as high as ~ 25 V on both the row and column electrode lines. Through proper shielding design, exceptionally low crosstalk between adjacent electrode lines is achieved, which gives an optimal near end crosstalk (NEXT) value of 0.01. A prototype of a visualized sensing system is demonstrated, which can display the position, the trajectory and the approximate profile of multiple contact objects in real time. The ITESA presented in this work does not rely on power supplies and possesses great flexibility as well as robustness. It can be scaled in area and is expected to be used in fields such as robotics, security monitoring, industrial automation, artificial intelligence, and health monitoring.

1. Introduction

A touch sensor is a type of device that acquires tactile information through physical touch [1]. It can measure the parameters that characterize a contact and has been widely utilized in such fields as robotics, security monitoring, industrial automation, artificial intelligence, and health monitoring [2,3]. Conventional technical routes for touch sensors include piezoelectric [4–6], piezoresistive [7–9] and capacitive [10–12] approaches. However, most touch sensors are based on semiconductor materials [11–20], such as silicon and gallium, which is mechanically fragile. Although a variety of flexible touch sensors has been reported in the past decade [21–24], they relied on specific materials and fabrication process, which largely prevented the area of the device from being scaled up. Furthermore, all of the aforementioned sensors require a sustained power supply, which brings about the problem of power consumption [25].

Recently, a novel sensing mechanism based on the coupling between triboelectrification and electrostatic induction has been reported [26]. The so-called triboelectric sensor can convert an external motion signal into an electrical signal that can be measured and analyzed [27].

This type of sensor normally uses flexible thin-film polymer materials and has advantages such as high sensitivity, zero power consumption and simple fabrication [28–30], making it suitable for wearable electronics. However, previously reported triboelectric sensors usually had the problem of cross talking [31–33], which was attributed to the electrostatic induction among sensing units [34]. This problem limits the triboelectric sensor for uses in precisely identifying the position of a contact object, especially when high-resolution mapping is required. Besides, multiple-point sensing has not been demonstrated by previous triboelectric sensors [35–38].

Herein, we report a fabric-based self-powered integrated triboelectric sensor array (ITESA) that can be scalable in area. Individual sensing units are constituted by intersections between row electrode lines and column electrode lines that have complementary patterns. When a specific sensing unit is touched, an output voltage of ~ 25 V is generated on corresponding row and column electrode lines. Possible crosstalk was effectively suppressed by a shielding layer. An optimal near end crosstalk (NEXT) value of 0.01 is achieved. A prototype system for visualized sensing is demonstrated, which can distinguish the position, trajectory and approximate profile of external contact objects,

* Corresponding authors at: Beijing Institute of Nanoenergy and Nanosystems, Chinese Academy of Sciences, Beijing 100083, China.
E-mail addresses: zhuguang@binn.cas.cn (G. Zhu), zlwang@binn.cas.cn (Z.L. Wang).

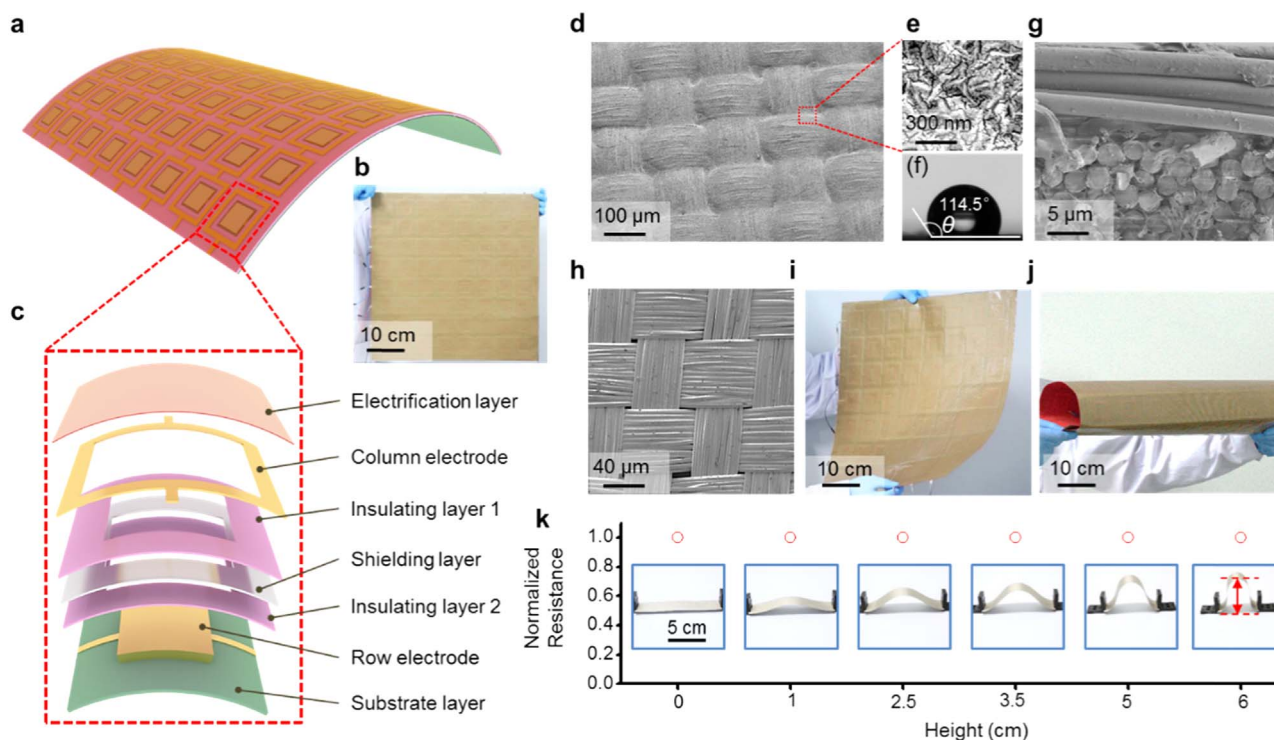


Fig. 1. Structural illustration of the integrated triboelectric sensor array (ITESA). (a) Schematic diagram of the ITESA in an eight by eight array. (b) Photograph of the as-fabricated ITESA. (c) A breakdown diagram of a single sensing unit. (d) Surface morphology of the electrification material in SEM image and in (e) an enlarged view. (f) Contact angle of the electrification material. (g) Cross-sectional view of the woven PTFE fabric. (h) SEM image of the woven conductive fabric. Photographs of (i) a bent and (j) a rolled ITESA. (k) Normalized resistance of the electrode material at different bending curvature.

such as hands and shoes. The ITESA reported in this work is expected to be used in fields such as security monitoring, indoor positioning, artificial intelligence and health monitoring.

The schematic diagram of the ITESA is shown in Fig. 1(a). It consists of 64 sensing units in an eight-by-eight array. The as-fabricated ITESA is presented in Fig. 1(b) with an area of $60 \times 60 \text{ cm}^2$. The breakdown structure of a single unit is shown in Fig. 1(c). The top layer is an electrification material made of polytetrafluoroethylene (PTFE) textile, which gains significant negative triboelectric charges upon contacting with other materials [26]. Two layers of electrodes are laid underneath the electrification material in separate layers. The column electrode layer is composed of individual units of hollow squares that are lined up in columns, while the row electrode layer consists of solid squares that are connected in rows. Each layer has an array of eight electrode lines. Because the column electrode lines are perpendicular to the row electrode lines, the intersections form a total of 64 sensing units. Between the two electrode layers, a shielding layer made of nickel-deposited conductive fabric is used and electrically grounded. Having a shape of hollow square, a unit of the shielding layer has a feature size smaller than the column electrode but larger than the row electrode. The detailed dimensions of each layer is presented in Supporting Fig. S1. The shielding layer significantly eliminates the electrostatic induction both between the two electrode layers in the vertical direction and among adjacent electrode lines on the same layer in the lateral direction. As a result, crosstalk can be largely eliminated, which will be discussed in details below. Two insulating layers that lie between the shielding layer and the electrode layers prevent electric shorts. The entire device is constructed on top of a flexible substrate made of non-woven fabric. The surface morphology of the electrification layer in scanning electron microscope (SEM) image is shown in Fig. 1(d). The enlarged view is presented in Fig. 1(e). The surface of the PTFE textile is hydrophobic in nature, which has a contact angle of 114.5° , as exhibited in Fig. 1(f). The hydrophobicity ensures that the ITESA is water proof. The cross-sectional view of the PTFE textile in Fig. 1(g) shows that the bundled

yarns are perpendicularly intertwined. Fig. 1(h) is the SEM image of the electrode material, which is essentially woven fabric deposited with copper and nickel. As shown in Fig. 1(i) and (j), the as-fabricated eight-by-eight sensor array can be easily bent and rolled, respectively, showing its great flexibility. The dependence of the electrical resistance of the electrode material on its curvature is revealed in Fig. 1(k). Here, the peak height of the bent sample is an indicator of the curvature [39]. The negligible fluctuation of the electrical resistance demonstrates excellent robustness and stability of the electrode material for its use in a flexible device.

The basic sensing principle of the ITESA relies on the conjunction of triboelectrification and electrostatic induction between the ITESA and an external contact object. As the object has dynamic interaction with the ITESA, the electrode lines experience measurable variation of electric potential. To elaborate this process, a three-dimensional model of three-by-three array was built, in which the electric potential distribution is numerically simulated *via* finite element method (FEM). The size of a contact object is set to be equivalent to that of a sensing unit. Detailed parameters of the model are discussed in the Methods. Assuming that the contact object is at the center of the three-by-three array, the obtained three-dimensional electric potential distribution is plotted in Fig. 2(a). The corresponding static distributions of electric potential for individual components of the ITESA are shown in Fig. 2(b) to (h). Here, particular discussions are focused on three components, *i.e.* the column electrode layer, the shielding layer, and the row electrode layer. For the column electrode layer shown in Fig. 2(d), the electrode line labeled as Y_2 on which the contact object locates has an electric potential of -35.2 V , which is significantly higher than that of adjacent electrode lines. Similarly, the electrode line labeled as X_2 has a substantially higher electric potential than that of the adjacent ones in the row electrode layer, as shown in Fig. 2(h). The observed significant difference is attributed to the shielding layer. As shown in Fig. 2(f), the shielding layer has a uniform electric potential of 0 V because it is grounded. It plays a key role in reducing crosstalk among adjacent

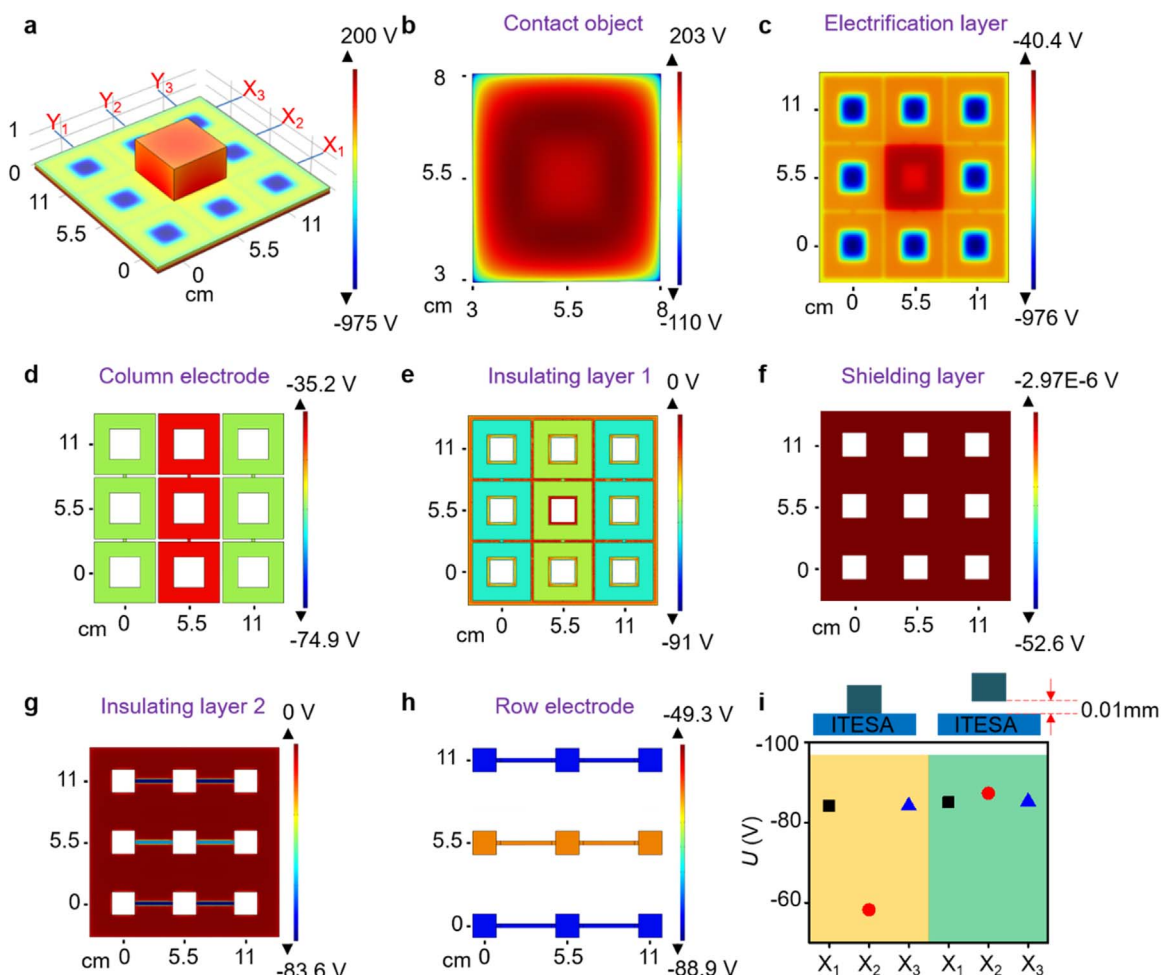


Fig. 2. Electric potential distribution of the ITESA calculated by COMSOL. (a) Overview of the electric potential distribution of the three-by-three sensor array when in contacting with an object. (b)–(h) Electric potential distribution of the contact object, the electrification layer, the column electrode layer, the first insulating layer, the shielding layer, the second insulating layer, and the row electrode layer, respectively. (i) U of the electrode lines X_1 , X_2 , and X_3 as the contact object is contact with the ITESA (left-handed section) and stays away from the ITESA at distance of 0.01 mm (right-handed section).

sensing units. Here, we define parameters U and ΔU to describe the electric potential and the change of the electric potential on an electrode line, respectively. We take the electrode lines X_1 , X_2 and X_3 as examples to illustrate the sensing process. The left-handed section of Fig. 2(i) shows the electric potential of the above three electrode lines when the contact object is in touch with the ITSEA. As the contact object starts to move away in the vertical direction, the values of the electric potential vary accordingly, which is shown in the right-handed section of Fig. 2(i). The variation of the electric potential can be expressed as

$$\Delta U = U_0 - U_x \tag{1}$$

where U_0 is the electric potential when the object is in contact with the electrification layer and U_x is the electric potential at a certain separation distance, i.e. 0.01 mm in Fig. 2(i). During electric measurement, an electrode line of the ITSEA is connected to the positive terminal of an electrometer (Keithley 6514, TEKTRONIX, INC.), while the negative terminal of the electrometer is grounded. As a result, the ΔU becomes the voltage signal that is actually measured. In the case shown in Fig. 2(i), when the contact object moves away from the ITSEA at a separation distance of 0.1 mm, the electric potential of the electrode line X_2 changes from -58 V to -87 V with the ΔU of 29 V, while the electric potential of the adjacent electrode lines X_1 and X_3 remains almost unchanged. Here, NEXT is used to illustrate the difficulty of signal recognition, which can be expressed as

$$\text{NEXT} = \Delta U_n / \Delta U_s \tag{2}$$

where ΔU_s is the change of the electric potential of the electrode line underneath the contact position, and ΔU_n is the change of the electric potential of the other electrode lines [40]. The lower value of the NEXT is, the less crosstalk among the electrode lines is, and the easier the signal recognition is. The ΔU_s of the electrode line X_2 is about 100 times higher than the ΔU_n of the electrode lines X_1 and X_3 , therefore, the NEXT reaches 0.01, which represents the low difficulty of signal recognition and the low crosstalk. In this way, it can be recognized that the contact takes place at a position corresponding to the electrode line X_2 . It is to be noted that the crosstalk among the electrode lines is extremely small, which allows the position of the object to be precisely identified. This feature will be discussed in details below.

Numerical simulation *via* COMSOL is conducted to determine how the structural parameters can affect the measured ΔU . Here, the three-by-three arrayed model is again adopted. The ΔU values of all the electrode lines on both electrode layers are plotted in Fig. 3(a). It is noticeable that the electrode lines X_2 and Y_2 experience a substantial increase in the electric potential as the contact object moves away from the ITSEA. At a separation distance of 0.1 mm, the ΔU on the electrode lines X_2 and Y_2 reach ~ 30 V, while the electric potential of the other electrode lines only varies by approximately 0.3 V. The Fig. 3(a) indicates that the crosstalk between adjacent electrode lines is significantly suppressed and the NEXT is 0.01, which is attributed to the screening effect from the shielding layer. This layer not only inhibits

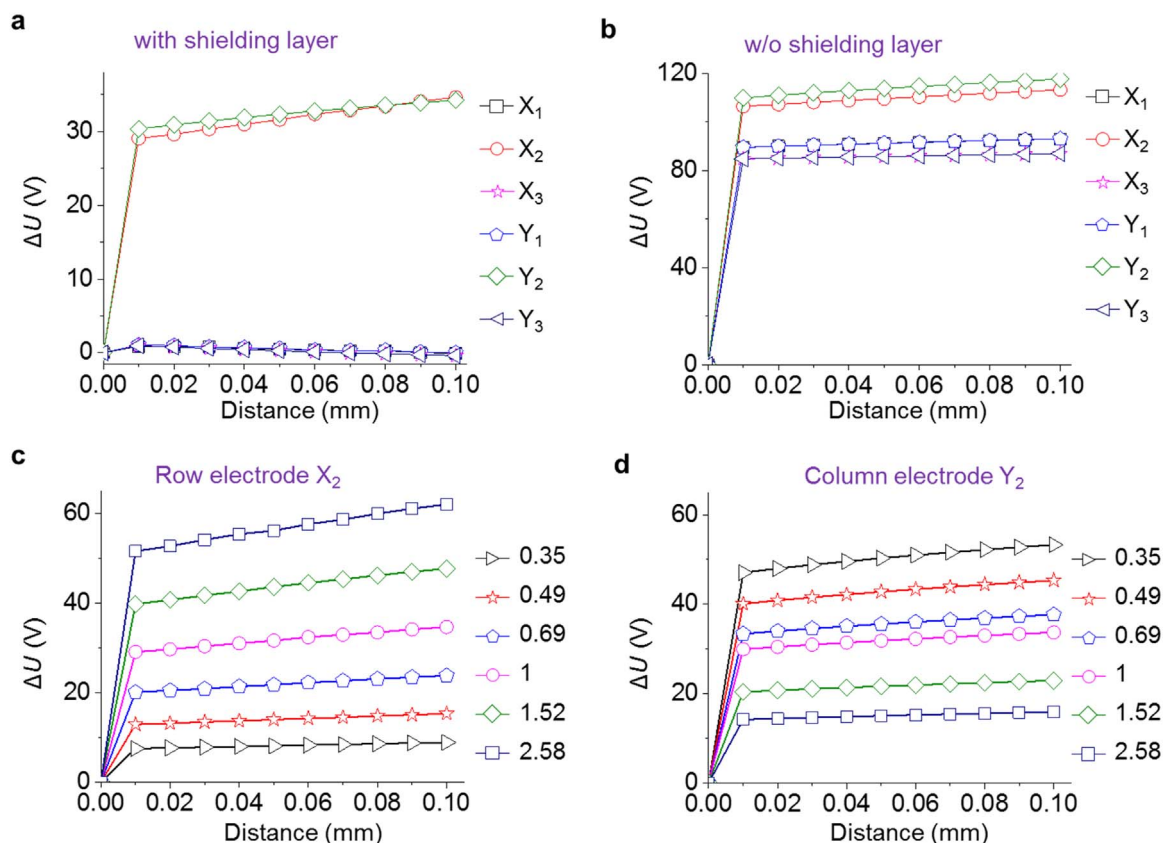


Fig. 3. Dependence of the ΔU on the distance between the contact object and the ITESA from numerical simulation. (a) ΔU of each electrode line if the ITESA has the shielding layer and (b) if the shielding layer is removed. (c) ΔU from the row electrode line X₂ and (d) from the column electrode line Y₂ at different ratio of the row electrode area to the column electrode area provided that the overall area of the ITESA keeps constant.

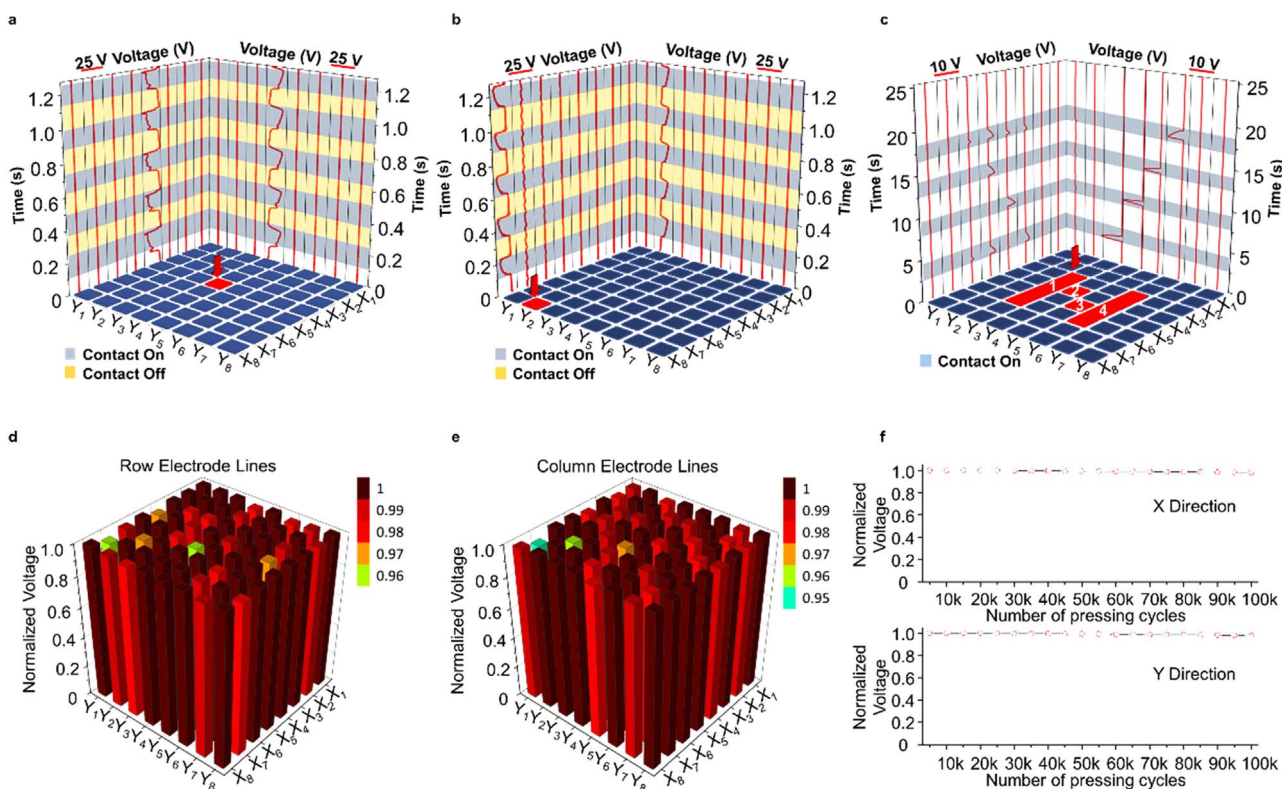


Fig. 4. Experimentally measured voltage signal from the ITESA. (a) Voltage signal from each electrode line as a contact object repeatedly interacts with a sensing unit at the center and (b) at the edge of the ITESA. (c) Voltage signal from each electrode line as multiple objects interact with the ITESA in a sequential way. (d) Normalized voltage signal from the row electrode lines and (e) from the column electrode lines. (f) Normalized voltage signal in a cyclic testing.

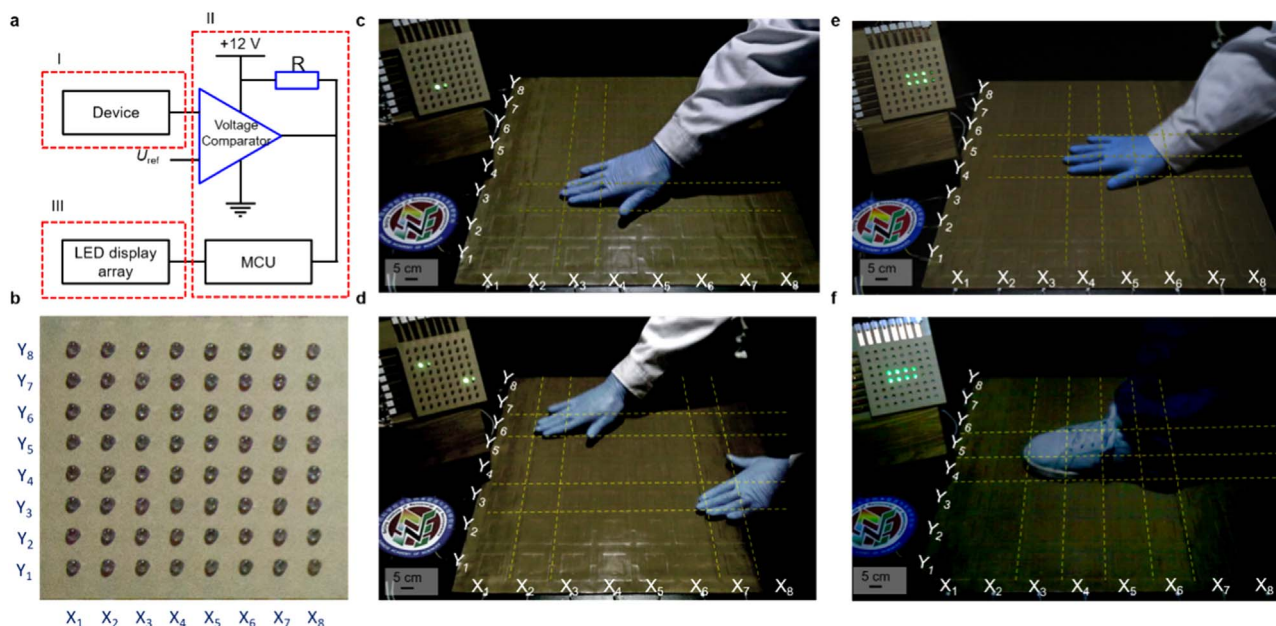


Fig. 5. Application demonstrations of the ITESA. (a) Electric circuit diagram of the sensing system. (b) Eight-by-eight LED-based display that has one-to-one correspondence with the sensing units of the ITESA. (c) ~ (f) Real-time visualized display of the sensing system for detecting single-point contact, multi-point contact, hand contact and shoe contact, respectively.

electrostatic induction between adjacent electrode lines in the same horizontal layer, but by also prevents vertical electrostatic induction between the row electrode layer and the column electrode layer. In a control group in which the shielding layer is removed, severe crosstalk can be observed, as shown in Fig. 3(b). For the case without the shielding layer, because the ΔU on all of the electrode lines have comparable values, and the NEXT is ~ 0.82 , it becomes difficult to pinpoint the position of the contact object. Therefore, the shielding layer plays a critical role in revealing the actual position of the contact object. This is a key feature that promises the ITSEA as an approach for high-resolution mapping in which a clear-cut boundary needs to be revealed.

The ΔU was found to be dependent on the area ratio of the row electrode area to the column electrode area. Here, we only discuss the ΔU on the electrode lines X_2 and Y_2 to determine the influence of the area ratio. As the area of the solid square pattern of the row electrode increases while the overall area of the ITSEA keeps constant, the ΔU on the row electrode line X_2 increases proportionally, as shown in Fig. 3(c). This is because triboelectrification is an area-dependent effect, increasing the area means the generation of more surface and thus higher electric potential. Accordingly, the ΔU of the column electrode line Y_2 decreases as the area of the open square pattern shrinks. The optimal ratio is found to be 1 as the ΔU on the electrode lines X_2 and Y_2 has closely comparable values, which ensures uniformly of the electric signal from the ITSEA.

The experimental results of the electric measurement on the eight-by-eight arrayed ITSEA is presented in Fig. 4. Firstly, a single-point contact test was conducted at the position indexed as (X_4, Y_4) , which corresponds to the intersection between the row electrode line X_4 and the column electrode line Y_4 . Repeated contacts occurs at a frequency of 4 Hz. The measured voltage signal on all of the 16 electrode lines is presented in Fig. 4(a). Five cyclic contacts induces cycled patterns of the voltage signal in a square wave, which are observed on both the electrode line X_4 and the electrode line Y_4 . The amplitude of the voltage variation reaches ~ 25 V and the NEXT keeps 0.01, which is consistent with the theoretically calculated values presented in Fig. 3(a). It can be observed that the voltage signal on all other electrode lines remains unchanged despite of the repeated contacts, which proves the effectiveness of the shielding layer in preventing the crosstalk. Secondly, the single-point contact test was conducted at the edge of the ITSEA with a

coordinate of (X_8, Y_2) , the repeated contacts produced periodic voltage variation on the electrode lines X_8 and Y_2 with similar amplitude of ~ 25 V. Again, the voltage signal is not observed on adjacent electrode lines. As for multi-point contact test, it was conducted at four different regions in a sequential way. The first contact occurs at the region labeled as “1” in Fig. 4(c). This bar-shaped object generates voltage signal on the column electrode line Y_3 as well as a series of row electrode lines from X_3 to X_6 . It is noticed that the voltage amplitude on different electrode lines (i.e. from X_3 to X_6) seems to be not uniform. For example, the electrode lines X_4 and X_6 correspond to significantly higher voltage amplitude. This is likely attributed to the fact that the bar-shaped object has a slightly curved surface, which prevented uniform contacts on all of the sensing units. It is also worth noting that the obtained voltage signal in Fig. 4(c) has a triangle wave rather than a square wave in the aforementioned cases. This is because the data acquisition in the multi-point test was accomplished by a multi-channel voltage meter (PXIe 4300, National Instruments Corporation), which has a substantially lower impedance than an electrometer. The multi-channel voltage meter is a resistive measuring equipment while the electrometer is a capacitive measuring equipment, as a result, the voltage signal is transient instead of being constant. The subsequent three contacts then take place at the regions labeled as 2, 3 and 4 in a sequential way. Because the voltage signal recorded in Fig. 4(c) can resolve both position and time, the overall trajectory of the multiple contacts can be then derived, which sets the basis for the application of the ITSEA in monitoring a moving object. Furthermore, the area uniformity and stability of the ITSEA are characterized. Fig. 4(d) and (e) present the normalized amplitude of the voltage signal on all of the row electrode lines and the column electrode lines, respectively. Each bar represents the obtained voltage amplitude as single-point contact is performed on corresponding sensing unit. The maximum variation throughout all of the sensing units is found to be not more than 5%, which proves excellent uniformity of the ITSEA. Fig. 4(f) demonstrates exceptional stability of the ITSEA, in which the voltage amplitude from a row electrode line and a column electrode line keeps unchanged after 100k repeated contacts at a frequency of 10 Hz.

To demonstrate practical applications of the ITSEA, we built up a prototype of a visualized sensing array system. As diagrammed in Fig. 5(a), this sensing system consists of three major parts, an eight-by-eight ITESA, a signal processing circuit, and a display panel composed

of an eight-by-eight LED-based array (Fig. 5(b)). When a sensing unit is triggered, the signal processing circuit scans the electric signal from all electrode lines and compares its value with a reference voltage (U_{ref}). Once the difference between the acquired voltage signal and the U_{ref} reaches a pre-set threshold, the microcontroller unit in the circuit switches on a LED that is at the position in correspondence to the sensing unit. As a result, the position, the trajectory and the shape of a contact object can be reflected by the LEDs that are switched on. Fig. 5(c) demonstrates the real-time sensing result of a single-point contact, in which a sensing unit is gently tapped by fingers (also presented in Supporting Movie S1). It can be observed that the ITSEA occasionally may not respond to the contacts. This is likely to be attributed to the fact that the contact area from the fingers may not be large enough to cover the column electrode and the row electrode at the same time. As a result, the sensor unit cannot be triggered. For multi-point contact, Fig. 5(d) and Supporting Movie S2 show that multiple positions of the contacts can be explicitly revealed on the display panel. Because this system can recognize multiple-contacts, it has the potential to identify the profile of a contact object. As presented in Fig. 5(e) and (f), regardless of whether the contact object is a hand palm or a shoe, the display panel can reflect not only the position but also the approximate profile of the contact object. These two demonstrations are also presented in Supporting Movies S3 and S4, respectively. Besides, the moving trajectory can be explicitly reflected, as shown in Supporting Movie S5. It is worth of noting that no power source is supplied onto the ITESA. When the sensing system is standing by, only extremely small current of μA is required to maintain the operation of the signal processing circuit. Therefore, the sensing system has significantly low power consumption. When contacting with diverse types of materials, the ITESA can be still properly functional. This is because the PTFE is the most negative material for triboelectrification so that considerable ΔU can be still produced and recognized by the signal-processing circuit.

Supplementary material related to this article can be found online at <http://dx.doi.org/10.1016/j.nanoen.2017.09.025>

2. Conclusion

The ITESA demonstrated in this work has a number of unique features and merits. Foremost, the thin-film polymeric materials and the layer-by-layer structure are compatible with area-scalable and cost-effective fabrication techniques. In this regard, the ITESA provides a facile method for touch sensing either in a large area or possibly in a small area with high resolution. On one hand, the ITESA has promising applications in security and surveillance for smart buildings when using in a large area. For example, as it is made of textile materials, the ITESA can be integrated into a smart carpet that can record when, where and how people in a room interact with the floor. This is especially useful for taking care for elderly and handicapped people. When abnormal events such as falls occur, the ITESA can immediately respond by identifying abnormal contact area and then sending out an alert. On the other hand, the ITESA may provide a novel path to realizing high-resolution mapping for uses such as fingerprint and footprint recognition. This is because the ITESA reported in this work demonstrates exceptionally low crosstalk and the ability of recognizing multiple points. Moreover, the voltage signal is directly generated through the conversion of mechanical energy into electrical energy. As a result, the ITESA itself does not require a power source to maintain its operation. Besides, the ITESA proves to have great flexibility and robustness, which is a key advantage compared to conventionally adopted approaches.

In summary, we have developed a fabric-based flexible ITESA with an area-scalable design. Voltage output was produced by triboelectrification and electrostatic induction against the external contact object. Individual sensing units are constituted by intersections between row electrodes and column electrodes that have complementary patterns. Low crosstalk was achieved with the use of a shielding layer.

Together with a signal processing system and an LED-based array display, an eight by eight pixelated sensing array was demonstrated and used to distinguish the position, trajectory and approximate shape of objects in external object contact with the device. We believe that this sensor array has significant potential for future development in the fields of security monitoring, industrial automation, artificial intelligence and health monitoring.

3. Experimental section

3.1. Fabrication of an ITESA

The ITESA was fabricated through a laser cutting machine (Pls. 75-50, Universal Laser System). A non-woven fabric was used as a substrate. The laser cutting machine was adopted to tailor the conductive fabric (Dongguan Shuishi Inc.) in order to create patterns of the row electrode layer, the column electrode layer and shielding layer. PTFE fabric (DuPont Inc) was selected as the electrification layer. All of the components were pasted together sequentially according to the order shown in Fig. 1(b).

3.2. Electric measurement

An electrometer (Keithley 6514, TEKTRONIX, INC.) was used to acquire the electric signal when single-point tests were conducted, and a multi-channel system (PXIe 4300, National Instruments Corporation) was used to simultaneously obtain the electric signals from all the electrode lines for multi-point contacts. An LM339N voltage comparator chip and an STM32 microcontroller unit chip were used to build the signal processing circuit that acquires and processes the generated electric signal in the visualized sensing system.

3.3. COMSOL simulation

The outer square size of a single unit was set to be 50 mm long and 50 mm wide, the surface charge density on the electrification layer was set to be $8 \times 10^{-6} \text{ C/m}^2$. The side length of the row electrode ranged from 22.5 to 35 mm, and the pore size of the column electrode ranged from 32.5 to 45 mm.

Acknowledgements

This research was supported by the National Key R&D Project from Ministry of Science and Technology, China (Grant no. 2016YFA0202701), National Science Foundation of China (Grant no. 51572030), and Beijing Natural Science Foundation (Grant no. 2162047).

Appendix A. Supplementary material

Supplementary data associated with this article can be found in the online version at <http://dx.doi.org/10.1016/j.nanoen.2017.09.025>.

References

- [1] V. Maheshwari, R.F. Saraf, *Angew. Chem. Int. Ed.* 47 (2008) 7808.
- [2] M.I. Tiwana, S.J. Redmond, N.H. Lovell, *Sens. Actuator A-Phys.* 179 (2012) 17.
- [3] P.S. Girão, P.M.P. Ramos, O. Postolache, J. Miguel Dias Pereira, *Measurement* 46 (2013) 1257.
- [4] W.Z. Wu, X.N. Wen, Z.L. Wang, *Science* 340 (2013) 952.
- [5] C. Pan, L. Dong, G. Zhu, S. Niu, R. Yu, Q. Yang, Y. Liu, Z.L. Wang, *Nat. Photon.* 7 (2013) 752.
- [6] W. Choi, J. Lee, Y.K. Yoo, S. Kang, J. Kim, J.H. Lee, *Appl. Phys. Lett.* (2014) 104.
- [7] L.J. Pan, A. Chortos, G.H. Yu, Y.Q. Wang, S. Isaacson, R. Allen, Y. Shi, R. Dauskardt, Z.N. Bao, *Nat. Commun.* (2014) 5.
- [8] S. Gong, W. Schwalb, Y.W. Wang, Y. Chen, Y. Tang, J. Si, B. Shirinzadeh, W.L. Cheng, *Nat. Commun.* (2014) 5.
- [9] C. Pang, G.Y. Lee, T.I. Kim, S.M. Kim, H.N. Kim, S.H. Ahn, K.Y. Suh, *Nat. Mater.* 11 (2012) 795.

- [10] D.J. Lipomi, M. Vosgueritchian, B.C.K. Tee, S.L. Hellstrom, J.A. Lee, C.H. Fox, Z.N. Bao, *Nat. Nano.* 6 (2011) 788.
- [11] J. Kim, M. Lee, H.J. Shim, R. Ghaffari, H.R. Cho, D. Son, Y.H. Jung, M. Soh, C. Choi, S. Jung, K. Chu, D. Jeon, S.T. Lee, J.H. Kim, S.H. Choi, T. Hyeon, D.H. Kim, *Nat. Commun.* (2014) 5.
- [12] S. Xu, Y.H. Zhang, L. Jia, K.E. Mathewson, K.I. Jang, J. Kim, H.R. Fu, X. Huang, P. Chava, R.H. Wang, S. Bhole, L.Z. Wang, Y.J. Na, Y. Guan, M. Flavin, Z.S. Han, Y.G. Huang, J.A. Rogers, *Science* 344 (2014) 70.
- [13] J. Viventi, D.H. Kim, L. Vigeland, E.S. Frechette, J.A. Blanco, Y.S. Kim, A.E. Avrin, V.R. Tiruvadi, S.W. Hwang, A.C. Vanleer, D.F. Wulsin, K. Davis, C.E. Gelber, L. Palmer, J. Van der Spiegel, J. Wu, J.L. Xiao, Y.G. Huang, D. Contreras, J.A. Rogers, B. Litt, *Nat. Neurosci.* 14 (2011) 1599.
- [14] N.S. Lu, C. Lu, S.X. Yang, J. Rogers, *Adv. Funct. Mater.* 22 (2012) 4044.
- [15] T.B. Xu, W.B. Wang, X.L. Bian, X.X. Wang, X.Z. Wang, J.K. Luo, S.R. Dong, *Sci. Rep.* (2015) 5.
- [16] C.T. Hong, L. Chu, W.C. Lai, A.S. Chiang, W.L. Fang, *IEEE Sens. J.* 11 (2011) 3409.
- [17] X.W. Wang, Y. Gu, Z.P. Xiong, Z. Cui, T. Zhang, *Adv. Mater.* 26 (2014) 1336.
- [18] Y.C. Lai, B.W. Ye, C.F. Lu, C.T. Chen, M.H. Jao, W.F. Su, W.Y. Hung, T.Y. Lin, Y.F. Chen, *Adv. Funct. Mater.* 26 (2016) 1286.
- [19] S. Chun, Y. Kim, H.S. Oh, G. Bae, W. Park, *Nanoscale* 7 (2015) 11652.
- [20] S. Chun, Y. Kim, H. Jung, W. Park, *Appl. Phys. Lett.* (2014) 105.
- [21] S.C.B. Mannsfeld, B.C.K. Tee, R.M. Stoltenberg, C.V.H.H. Chen, S. Barman, B.V.O. Muir, A.N. Sokolov, C. Reese, Z.N. Bao, *Nat. Mater.* 9 (2010) 859.
- [22] L. Persano, C. Dagdeviren, Y.W. Su, Y.H. Zhang, S. Girardo, D. Pisignano, Y.G. Huang, J.A. Rogers, *Nat. Commun.* (2013) 4.
- [23] M.A.S.M. Haniff, S.M. Hafiz, K.A.A. Wahid, Z. Endut, H.W. Lee, D.C.S. Bien, I.A. Azid, M.Z. Abdullah, N.M. Huang, S.A. Rahman, *Sci. Rep.* (2015) 5.
- [24] S. Yoon, J.K. Sim, Y.H. Cho, *Sci. Rep.* (2016) 6.
- [25] H.K. Kim, S. Lee, K.S. Yun, *Sens. Actuator A-Phys.* 165 (2011) 2.
- [26] F.R. Fan, Z.Q. Tian, Z.L. Wang, *Nano Energy* 1 (2012) 328.
- [27] Z.L. Wang, *ACS Nano*. 7 (2013) 9533.
- [28] B. Meng, W. Tang, Z.H. Too, X.S. Zhang, M.D. Han, W. Liu, H.X. Zhang, *Energ. Environ. Sci.* 6 (2013) 3235.
- [29] M. Ha, J. Park, Y. Lee, H. Ko, *ACS Nano*. 9 (2015) 3421.
- [30] G. Zhu, W.Q. Yang, T.J. Zhang, Q.S. Jing, J. Chen, Y.S. Zhou, P. Bai, Z.L. Wang, *Nano Lett.* 14 (2014) 3208.
- [31] Y. Yang, H.L. Zhang, Z.H. Lin, Y.S. Zhou, Q.S. Jing, Y.J. Su, J. Yang, J. Chen, C.G. Hu, Z.L. Wang, *ACS Nano*. 7 (2013) 9213.
- [32] Y.J. Su, G. Zhu, W.Q. Yang, J. Yang, J. Chen, Q.S. Jing, Z.M. Wu, Y.D. Jiang, Z.L. Wang, *ACS Nano*. 8 (2014) 3843.
- [33] F. Yi, L. Lin, S.M. Niu, J. Yang, W.Z. Wu, S.H. Wang, Q.L. Liao, Y. Zhang, Z.L. Wang, *Adv. Funct. Mater.* 24 (2014) 7488.
- [34] X.D. Wang, H.L. Zhang, L. Dong, X. Han, W.M. Du, J.Y. Zhai, C.F. Pan, Z.L. Wang, *Adv. Mater.* 28 (2016) 2896.
- [35] Q.J. Liang, X.Q. Yan, X.Q. Liao, S.Y. Cao, S.N. Lu, X. Zheng, Y. Zhang, *Sci. Rep.* (2015) 5.
- [36] Y.S. Zhou, G. Zhu, S.M. Niu, Y. Liu, P.S. Bai, Q. Jing, Z.L. Wang, *Adv. Mater.* 26 (2014) 1719.
- [37] W.Q. Yang, J. Chen, X.N. Wen, Q.S. Jing, J. Yang, Y.J. Su, G. Zhu, W.Z. Wu, Z.L. Wang, *ACS Appl. Mat. Interfaces* 6 (2014) 7479.
- [38] Y. Wu, Q.S. Jing, J. Chen, P. Bai, J.J. Bai, G. Zhu, Y.J. Su, Z.L. Wang, *Adv. Funct. Mater.* 25 (2015) 2166.
- [39] M.K. Shin, J. Oh, M. Lima, M.E. Kozlov, S.J. Kim, R.H. Baughman, *Adv. Mater.* 22 (2010) 2663.
- [40] J.C. Isaacs, N.A. Strakhov, *Bell Labs Tech. J.* 52 (1973) 101.